LETTER

doi:10.1038/nature12032

A conformational switch in HP1 releases auto-inhibition to drive heterochromatin assembly

Daniele Canzio[1,2], Maofu Liao[1], Nariman Naber[1], Edward Pate[3], Adam Larson[1,4], Shenping Wu[1], Diana B. Marina[1,4], Jennifer F. Garcia[1,4], Hiten D. Madhani[1], Roger Cooke[1], Peter Schuck[5], Yifan Cheng[1] & Geeta J. Narlikar[1]

A hallmark of histone H3 lysine 9 (H3K9)-methylated heterochromatin, conserved from the fission yeast *Schizosaccharomyces pombe* to humans, is its ability to spread to adjacent genomic regions[1–6]. Central to heterochromatin spread is heterochromatin protein 1 (HP1), which recognizes H3K9-methylated chromatin, oligomerizes and forms a versatile platform that participates in diverse nuclear functions, ranging from gene silencing to chromosome segregation[1–6]. How HP1 proteins assemble on methylated nucleosomal templates and how the HP1–nucleosome complex achieves functional versatility remain poorly understood. Here we show that binding of the key *S. pombe* HP1 protein, Swi6, to methylated nucleosomes drives a switch from an auto-inhibited state to a spreading-competent state. In the auto-inhibited state, a histone-mimic sequence in one Swi6 monomer blocks methyl-mark recognition by the chromodomain of another monomer. Auto-inhibition is relieved by recognition of two template features, the H3K9 methyl mark and nucleosomal DNA. Cryo-electron-microscopy-based reconstruction of the Swi6–nucleosome complex provides the overall architecture of the spreading-competent state in which two unbound chromodomain sticky ends appear exposed. Disruption of the switch between the auto-inhibited and spreading-competent states disrupts heterochromatin assembly and gene silencing *in vivo*. These findings are reminiscent of other conditionally activated polymerization processes, such as actin nucleation, and open up a new class of regulatory mechanisms that operate on chromatin *in vivo*.

HP1 has two structured domains, a chromodomain (CD) and a chromoshadow domain (CSD), connected by an unstructured hinge region (Fig. 1a). The CD recognizes the trimethylated H3K9 (H3K9me3) mark[7–9], whereas the CSD can homodimerize[10–12] and binds specific protein sequences[13,14]. The hinge is implicated in sequence-independent RNA and DNA binding[15,16]. Here we investigate how the key *S. pombe* HP1 protein Swi6 uses its different domains to create a regulatable HP1–chromatin complex.

It is proposed that heterochromatin spread relies on the ability of HP1 proteins to self-associate on chromatin[1,5]. To understand how Swi6 self-association is regulated by chromatin, we first characterized the individual oligomerization equilibria in the absence of nucleosomes using analytical ultracentrifugation (AUC). Previous work has characterized at least three Swi6 oligomeric states: a monomer, a dimer mediated by CSD–CSD interactions and higher-order oligomers mediated by CD–CD interactions between dimers[10,12,15,17,18]. Analysis of our AUC data best describes the system as a two-step self-association process: a tight association of two Swi6 monomers with an affinity constant, K_{obs}^{dim}, ($1/K_{obs}^{dim} < 1$ nM, at 8 °C), followed by progressive self-association of Swi6 dimers with an identical chain-elongation affinity constant, K_{obs}^{iso}, ($1/K_{obs}^{iso} \sim 70$ μM, at 8 °C) (dim indicates dimerization, iso indicates isodesmic and obs indicates observed; Fig. 1b–d and Supplementary Figs 1, 2 and 3). This second step, also known as isodesmic self-association, is analogous to the self-association of tubulin dimers[19].

We next tested whether the most distinguishing feature of the chromatin template, the H3K9 methyl mark, increases Swi6 oligomerization when it occupies the CD. An increase in oligomerization would be reflected by an increase in the overall weighted average sedimentation coefficient, s_w, of Swi6 as a function of H3K9me3 peptide (Fig. 1e). In contrast to our simplest expectation, addition of the methylated peptide reduced the value of s_w, implying that Swi6 self-association is inhibited by the methylated H3 tail peptide (Fig. 1e). This result suggested that the methylated H3 tail peptide and the CD–CD interface may compete for the same site. We noticed that the CD of Swi6 contains a sequence (92-Ala-Arg-Lys-Gly-Gly-Gly-97) on a loop that resembles the amino acid sequence of the H3 tail surrounding the Lys 9 position (7-Ala-Arg-Lys-Ser-Thr-Gly-12) (Fig. 1f). Interestingly, although the Swi6 sequence degenerates in higher organisms to just the lysine and proximal glycine (Fig. 1f), in human HP1 isoforms the lysine shows post-translational modifications found on H3K9, such as monomethylation and acetylation[20]. We therefore proposed that the ARK loop from the CD of one Swi6 could occupy the H3K9-binding site in another CD to mediate CD–CD self-association in solution (Fig. 1g). This is reminiscent of observations that the HP1 CD can bind ARK-containing motifs in histone H1 and G9a proteins[21,22].

To test this model, we investigated the effects of replacing the Arg 93 and the Lys 94 residues with alanines ($Swi6^{LoopX}$; Fig. 1g and Supplementary Table 1) on oligomerization. As predicted by the model, the $Swi6^{LoopX}$ mutant showed a small but reproducible (threefold) decrease in the isodesmic affinity constant (K_{obs}^{iso}) (Fig. 2a and Supplementary Fig. 4). Interestingly, we noticed a substantially larger (14-fold) reduction in the association constant for dimerization (K_{obs}^{dim}) (Fig. 2b and Supplementary Fig. 4). Thus, in addition to the previously identified CSD–CSD interface, the ARK loop–CD interaction also participates in stabilizing a Swi6 dimer. We further found that $Swi6^{LoopX}$ binds tail peptides approximately sixfold more strongly than wild-type Swi6 ($Swi6^{WT}$) (Fig. 2d), and that Swi6 dimerization is weakened with saturating methylated H3 tail peptide (Supplementary Fig. 4). These results indicate that the ARK loop–CD interaction is mutually exclusive with H3 tail binding.

The above data suggest that a Swi6 dimer can exist in at least two states: a closed state in which the ARK loop engages the CD of its partner Swi6 and an open state in which the ARK loop–CD interaction is broken (Fig. 2c). Self-association of dimers then consists of: (1) a conformational step between closed and open states (K^{conf}); and (2) a self-association step between dimers in the open state (K^{oligo}). For $Swi6^{WT}$ the measured isodesmic association step (K_{obs}^{iso}) is a product of K^{conf} and K^{oligo} (Fig. 2c). In $Swi6^{LoopX}$ the effect on dimerization masks the destabilizing effect of the loop mutations on the actual oligomerization step (K^{oligo}) (Fig. 2c).

[1]Department of Biochemistry and Biophysics, University of California San Francisco, California 94158, USA. [2]Chemistry and Chemical Biology Graduate Program University of California San Francisco, California 94158, USA. [3]Voiland School of Chemical Engineering and Bioengineering, Washington State University, Pullman, Washington 99164, USA. [4]Tetrad Graduate Program University of California San Francisco, California 94158, USA. [5]National Institute of Biomedical Imaging and Bioengineering, National Institutes of Health, Bethesda, Maryland 20892, USA.

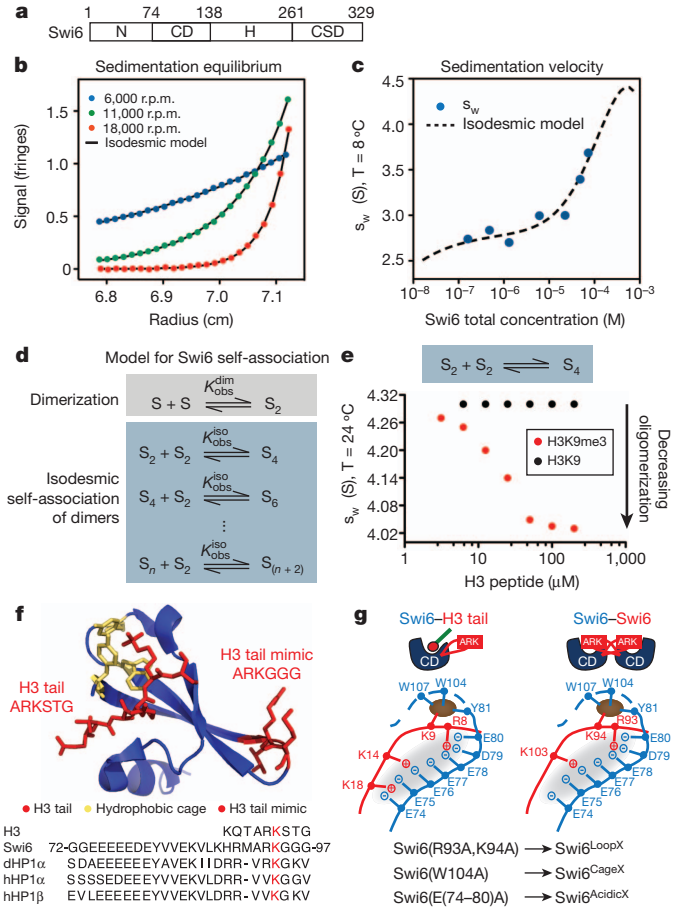

H3 KQTARKSTG
Swi6 72-GGEEEEEDEYVVEKVLKHRMARKGGG-97
dHP1α SDAEEEEEEYAVEKIIDRR-VRKGKV
hHP1α SSSSEDEEEYVVEKVLDRR-VVKGGV
hHP1β EVLEEEEEEYVVEKVLDRR-VVKGKV

Figure 1 | Dissecting Swi6 self-association equilibria. **a**, Swi6 domains. H, hinge; N, N-terminal region. **b**, Sedimentation equilibrium AUC analysis of $Swi6^{WT}$ self-association. Interference profiles at different rotor speeds are shown. Every twentieth point is shown. **c**, Sedimentation velocity AUC analysis of $Swi6^{WT}$ self-association. T, temperature. For **b** and **c**, best fits for global analysis using an isodesmic self-association model are shown. **d**, Model of Swi6 self-association. S, Swi6 monomer. **e**, $[Swi6^{WT}] = 20\ \mu M$. Sedimentation coefficients: dimer (S_2) = ~4 S; tetramer (S_4) = ~5.2 S. **f**, Top, Swi6 CD modelled on *Drosophila* HP1 CD with H3K9me3 peptide (Protein Data Bank (PDB) code, 1KNE). Bottom, H3 tail (amino acids 4–14) and CD loop regions of Swi6 (amino acids 72–97), *Drosophila* (d) HP1α and human (h) HP1α and HP1β. Conserved lysine in red. **g**, Top, models for CD–CD and CD–ARK loop interactions. H3 tail, green line; methylation, red circle. Middle, schematic of Swi6–H3 tail interactions (left) and of hypothetical CD–CD interactions (right). Grey oval, region of negative charge; brown oval, π-cation interactions. Bottom, mutants used.

To investigate the extent of similarity between the ARK loop–CD interaction and the H3–CD interaction, we used two additional mutants. The first is $Swi6^{CageX}$, in which an aromatic cage residue important for H3K9me3 binding[8] is mutated to alanine (Fig. 1g and Supplementary Table 1). The second is $Swi6^{AcidicX}$, in which an acidic stretch amino-terminal to the first aromatic cage residue of the CD is mutated to alanines (Fig. 1g and Supplementary Table 1; rationale in Supplementary Discussion). Both mutants show reduced binding to H3K9me3 peptides (Fig. 2d). These mutants also destabilize Swi6 oligomerization and dimerization (Fig. 2a, b and Supplementary Fig. 4), suggesting that similar interactions are involved in the H3–CD and ARK loop–CD interfaces (Fig. 1g).

We next used electron paramagnetic resonance (EPR) spectroscopy to ask whether disruption of the ARK loop–CD interface or binding of the H3K9me3 tail makes the loop more mobile by stabilizing the open conformation (Fig. 2c, e). Changes in the mobility of a site-specifically attached spin probe can give well-defined changes in its EPR spectrum[23]. We mutated all three native cysteines in Swi6 to serines ($Swi6^{3S}$; Supplementary Table 1), mutated the Gly 95 residue on the loop to a cysteine, and then modified it with a maleimide spin probe ($Swi6^{probe}$; Supplementary Table 1). Mutating the native cysteines destabilized oligomerization, H3 peptide binding and nucleosome binding (Supplementary Fig. 5), but the mutants still showed substantial discrimination for the H3K9 methyl mark (Supplementary Fig. 5).

Two spectral components were observed for $Swi6^{probe–WT}$, one with higher mobility and one with reduced mobility. Deconvolution of the two components gave the fraction of probes that are immobilized. In parallel, AUC experiments confirmed the oligomeric state of the protein. For the $Swi6^{probe–WT}$ protein, ~35% of the probes were immobile (Fig. 2f). Compared to $Swi6^{probe–WT}$, the fraction of immobile probes decreased in $Swi6^{probe–LoopX}$, $Swi6^{probe–AcidicX}$ and $Swi6^{probe–DimerX}$ (L315D; Supplementary Table 1), which disrupts CSD–CSD dimerization and increases monomeric Swi6 (ref. 18) (Fig. 2f and Supplementary Fig. 5). The values obtained for the mutants relative to wild type are consistent with our thermodynamic characterization (Fig. 2a, b). Further, as predicted by the model (Fig. 2c, e), addition of the H3K9me3 peptide decreased the fraction of immobile probes. The H3K9me3 peptide was ~100-fold better at decreasing the immobile probe fraction compared to both H3K9 and H3K4me3 peptides, indicating that the effect was specific for the H3K9me3 mark (Fig. 2g; additional mutants in Supplementary Fig. 5).

To investigate the global structure of Swi6 dimers, we used negative-stain electron microscopy. To increase the mass for visualization by electron microscopy, and to identify the N terminus of Swi6, we fused a cyan fluorescent protein (CFP) molecule to the N terminus of Swi6 (Fig. 3a and Supplementary Fig. 6). The CFP–Swi6 construct showed an extended conformation (Fig. 3a). We reasoned that the proximity of the CFP tag to the CD perhaps disrupts the ARK loop–CD interaction. Consistent with this reasoning, CFP–Swi6 forms a ~tenfold weaker dimer than $Swi6^{WT}$ (Fig. 2b and Supplementary Fig. 6). To maintain the ARK loop–CD interaction, we moved the CFP tag to the carboxy terminus (Fig. 3b). Swi6–CFP has a similar dimerization constant to $Swi6^{WT}$, consistent with having an intact ARK loop–CD interaction (Supplementary Fig. 6), shows a more condensed structure compared to CFP–Swi6 and has a lower sedimentation coefficient (Fig. 3b and Supplementary Fig. 6). These results raised the possibility that the extended conformation of CFP–Swi6 reflects the open state (Fig. 2c), which is capable of binding methylated nucleosomes. We therefore visualized Swi6 bound to a methylated nucleosome using cryo-electron microscopy, and for comparison, visualized nucleosomes alone (Fig. 3c). On the basis of our previous biochemical knowledge, we applied two-fold symmetry to the Swi6–nucleosome complex to obtain the three-dimensional reconstruction (see also Supplementary Methods). For the nucleosome and the Swi6–nucleosome complexes, three-dimensional reconstructions were calculated using the nucleosome structure as an initial model to an overall resolution of ~15 Å and ~25 Å, respectively (Fig. 3c, Supplementary Fig. 7 and Methods).

The 25 Å resolution of the Swi6–nucleosome complex precludes conclusions about the detailed conformations of the bound Swi6 dimers. We instead further analysed the difference density between the complex and nucleosome (Fig. 3c). Although we cannot rule out that Swi6 binding alters nucleosome conformation, the difference density has roughly the mass (~125 kDa) of two Swi6 dimers (~150 kDa) as determined previously[18]. We thus assume that the difference density is mainly contributed by the bound Swi6 dimers. The putative location of the CD suggests that one CD engages an H3 tail and one CD protrudes out in solution (Fig. 3d). This arrangement of the CDs is compatible with the sticky ends architecture proposed previously[18] (Fig. 3e). The putative location of the CSD dimer suggests that this domain may also engage the nucleosome (Fig. 3c, d). This possibility has also been previously suggested[24–26]. To test it directly, we measured binding of the $Swi6^{DimerX}$ to methylated nucleosomes, and observed that disruption of the CSD dimer decreases binding by tenfold (Fig. 4a and Supplementary Fig. 8).

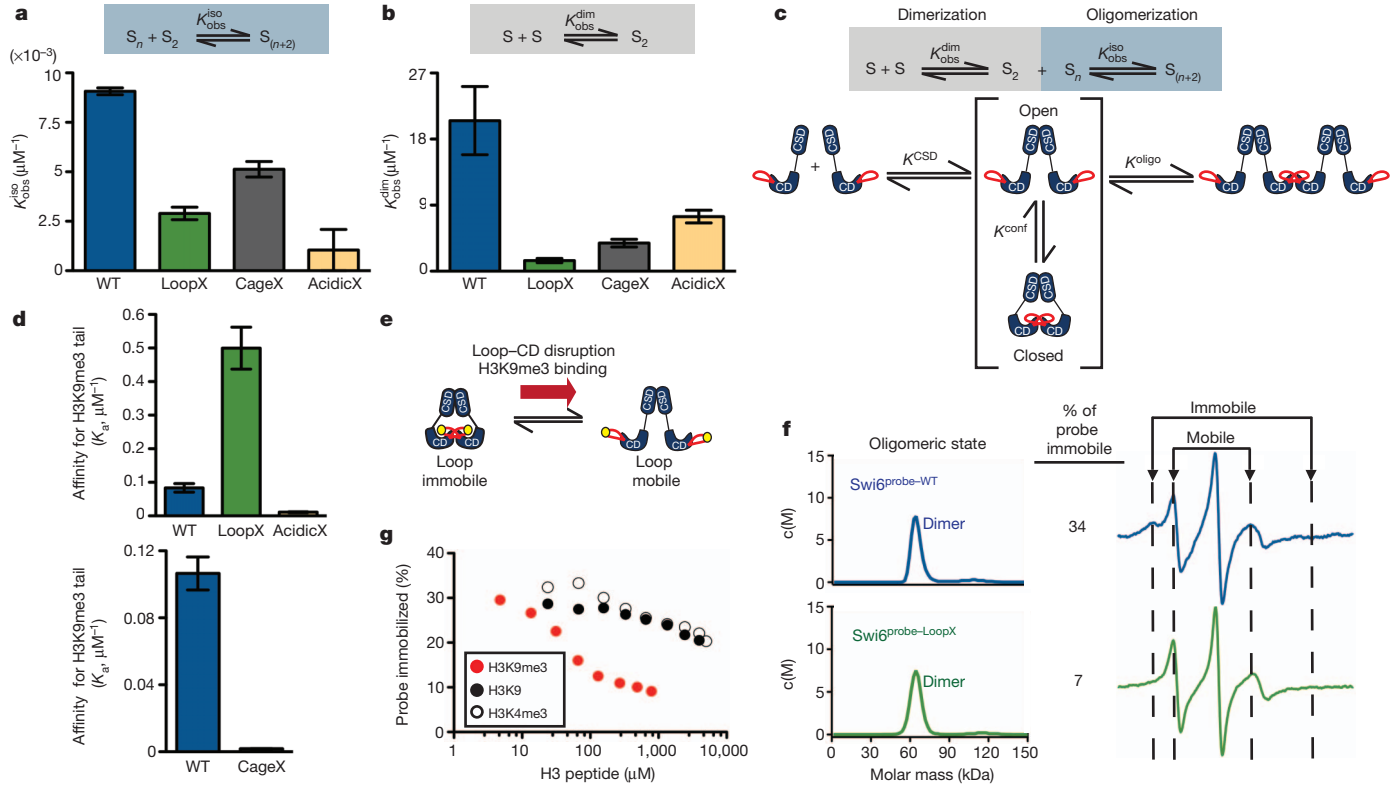

Figure 2 | Impact of disrupting H3 tail mimic–CD interaction. **a**, **b**, Isodesmic association constant (K_{obs}^{iso}) (**a**) and dimerization association constant (K_{obs}^{dim}) (**b**) for Swi6 mutants (values in Supplementary Fig. 4). **c**, Model for the self-association of Swi6. (K^{conf} = [open]/[closed]). K^{oligo} is the isodesmic association constant for oligomerization from the open state. For $Swi6^{WT}$, $K_{obs}^{dim} = \frac{K^{CSD}}{K^{conf}}$ and $K_{obs}^{iso} = K^{conf} \times K^{oligo}$. **d**, Affinity constants (K_a) for H3K9me3 tail peptide measured by tryptophan fluorescence (top) and fluorescence anisotropy (bottom) studies (values in Supplementary Fig. 8). **e**, Location of MSL (4-maleimido-2,2,6,6-tetramethyl-1-piperidinyloxy) probe on G95C (yellow circle). **f**, Sedimentation velocity AUC (left panels) and EPR analyses (right panels) of $Swi6^{probe–WT}$ and $Swi6^{probe–LoopX}$. Representative EPR spectra shown as derivative of absorbance (*y* axis) versus magnetic field (*x* axis). c(M), molar mass distribution. Errors for probe immobilized <10%. **g**, Impact of 18-nucleotide H3 peptides on probe immobilization. $[Swi6^{probe–WT}] = 20\ \mu M$. For all panels, error bars represent s.e.m. ($n \geq 3$).

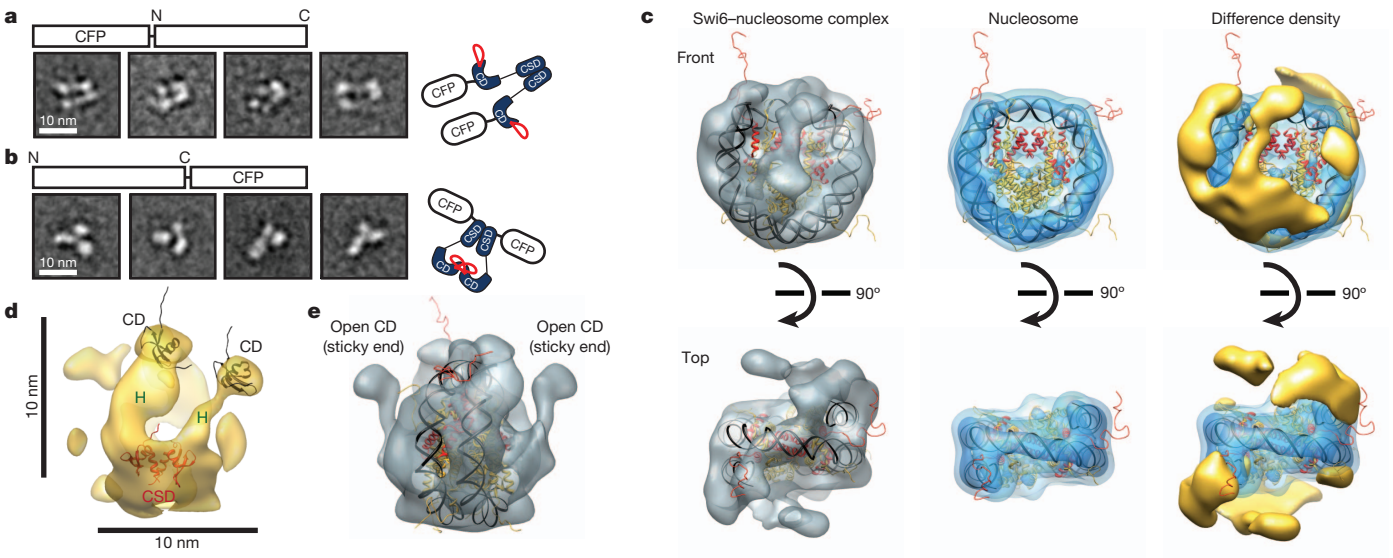

Figure 3 | Electron microscopy studies of Swi6 and Swi6–H3K_C9me3 nucleosome complex. **a**, **b**, CFP–Swi6 (**a**) and Swi6–CFP (**b**). Representative two-dimensional class averages are shown. **c**, Two different views of three-dimensional reconstruction of the Swi6–H3K_C9me3 (K_C indicates derivation of this analogue by alkylation of a cysteine residue, see Methods) nucleosome complex (left), nucleosome (middle) and difference map between the two reconstructions (right). Nucleosome crystal structure (PDB code, 1KX5) was fitted into reconstruction. Isosurface of nucleosome three-dimensional reconstruction at high threshold in dark blue and low threshold in light blue (nucleosome type used in Methods). H3, red; difference map, yellow. **d**, Putative locations of Swi6 domains docked into difference map: CD of Swi6 (black; PDB code, 2RSO; amino acids 72–142), CSD domain of Swi6 (red; PDB code, 1E0B) and hinge (H). **e**, Proposed locations of the two unoccupied CDs.

Surprisingly, in contrast to the results with the H3 tail peptides (Fig. 2d), disrupting auto-inhibition through the Swi6^{LoopX} mutant reduced binding to methylated nucleosomes by tenfold, even though discrimination for the methyl mark was maintained (Fig. 4a and Supplementary Fig. 8). This suggested that, when displaced from the CD, the ARK loop may help Swi6 make additional interactions with the nucleosome. We tested whether the positively charged ARK loop assists interactions with DNA. We found that Swi6^{WT} binds ~fourfold tighter than Swi6^{LoopX} to a 20-base pair DNA duplex (Fig. 4b). Further, Swi6^{WT} bound to the DNA ~fourfold tighter with saturating H3K9me3 peptide, consistent with the loop being available when displaced from the CD (Fig. 4b and Supplementary Fig. 8). In contrast to Swi6^{LoopX}, Swi6^{AcidicX}, which binds H3K9me3 peptides more weakly than Swi6^{WT}, also binds methylated nucleosomes ~sevenfold more weakly (data not shown).

On the basis of the above data, we propose that binding to methylated nucleosomes has two coupled effects: (1) release of ARK loops to directly or indirectly help DNA binding; and (2) release of two CDs that can bridge nearby nucleosomes (Fig. 4c). This new model revises our previously proposed model[18] (see Supplementary Discussion). Our data imply that the cooperative action of the CD, the CSD–CSD dimer and the ARK loop couples the assembly of Swi6 to the recognition of specific features of the nucleosomal template such as H3K9 methylation and nucleosomal DNA. This coupling can ensure correct targeting to H3K9-methylated chromatin and reduce aberrant spread in euchromatin. Interestingly, the loop that stabilizes the auto-inhibited state assists in binding nucleosomes when in the open state. These mutually exclusive roles of the loop may enable switch-like behaviour in HP1 spreading.

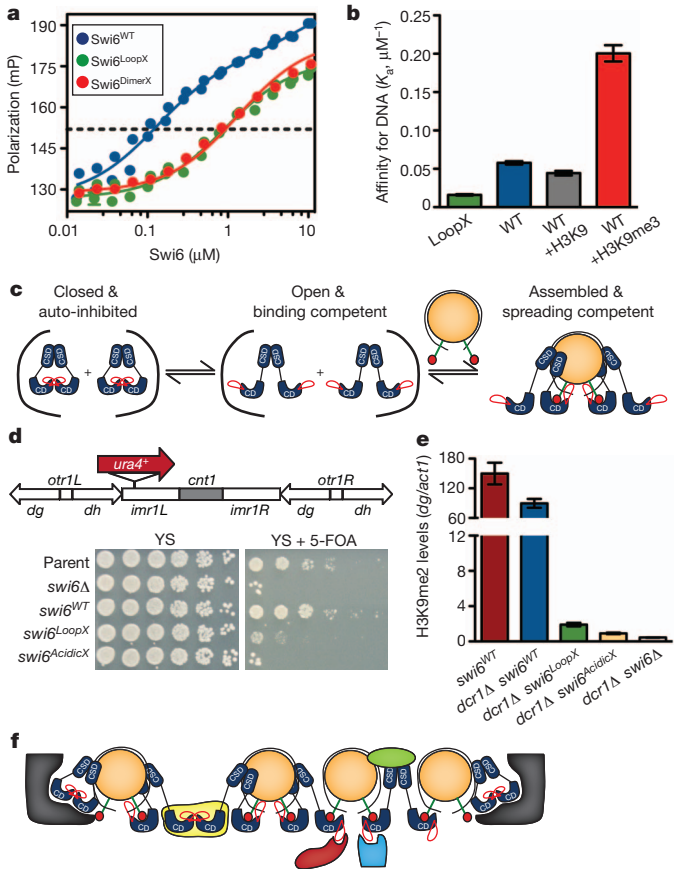

Figure 4 | Nucleosome recognition and *in vivo* impact of disrupting loop–CD interaction. **a**, **b**, Nucleosome binding assayed by fluorescence anisotropy (**a**) and affinity constants for 20-base-pair DNA (**b**). K_d values are in Supplementary Fig. 8. Error bars represent s.e.m. ($n \geq 3$). mP, millipolarization units. **c**, Model for conformational switch in Swi6 upon binding methylated nucleosomes. **d**, Top, schematics of centromere 1 showing *ura4*$^+$ reporter. cnt, centromere; L, left; otr, outer-most repeats; R, right. Bottom, silencing assay using *ura4*$^+$ reporter. **e**, *swi6*^{LoopX} and *swi6*^{AcidicX} mutants decrease H3K9 methylation levels at the centromeric *dg* on a *dcr1*Δ background. Error bars denote s.e.m from three independent immunoprecipitations. **f**, Model depicts how conformational versatility of the HP1–chromatin platform enables recruitment of diverse regulators that promote (yellow, red, blue and green cartoons) or inhibit (grey cartoon) heterochromatin spread.

To test the relevance of this model *in vivo*, we investigated the impact of the LoopX and AcidicX mutants in assembling a functional heterochromatin structure. As these mutants concomitantly weaken oligomerization and nucleosome binding, we expected to observe loss-of-function effects *in vivo*. We first investigated effects on the silencing of a *ura4*$^+$ reporter gene inserted at the pericentromeric *imr* (innermost repeat) region (Fig. 4d). Both mutants show defects in silencing that are comparable to the *swi6*$^+$ deletion strain and that are not due to reductions in protein levels (Fig. 4d and Supplementary Fig. 9). Next, we investigated effects at endogenous centromeric *dg* repeats. In the absence of the RNA interference (RNAi) machinery, Swi6 is important for maintaining high levels of H3K9 methylation at *dg* repeats[27]. Although deletion of RNAi components causes a small but reproducible decrease in H3K9 methylation, further deletion of *swi6* causes a much larger decrease in H3K9 methylation[27]. We find that the *loopX* and *acidicX* mutants also show large decreases in H3K9 methylation in the absence of an RNAi component such as dicer (*dcr1*) (Fig. 4e and Supplementary Fig. 9). These data imply that the ARK loop–CD interaction is important for the integrity of H3K9-methylated heterochromatin *in vivo*. Our results with the LoopX and AcidicX mutants are also consistent with previous work showing that mutations in these regions affect mitotic stability and mating type switching[17], both of which depend on the integrity of heterochromatin.

The ability of Swi6 to exist in more than one discrete conformational state may allow it to interact with different regulators through the CSD–CSD interface, the hinge or the ARK loop, and this could alter the stability and structure of the Swi6–nucleosome platform (Fig. 4f). The Ala-Arg-Lys-Gly-Gly-Gly sequence is absent in the other *S. pombe* HP1 protein, Chp2, and this difference may in part explain the different biological roles of Chp2 and Swi6 (ref. 28). In Swi6, the ARK loop stabilizes the auto-inhibited state even though the lysine is not methylated, presumably due to the high effective concentration of the ARK loop relative to its partner CD. However, human HP1α contains just the Lys-Gly residues of the Ala-Arg-Lys-Gly-Gly-Gly sequence and, in this context, the lysine can be monomethylated *in vivo*[20]. It is tempting to speculate that the methylation energetically compensates for the loss of the arginine while also making the interaction more regulatable. Protein assemblies that are controlled by release of auto-inhibition have been well characterized in processes such as actin nucleation and protein tyrosine kinase activation[29,30]. We anticipate that similarly sophisticated mechanisms govern the assembly, spread and functions of HP1-mediated heterochromatin.

METHODS SUMMARY

Swi6 was purified from *Escherichia coli* as described previously[18]. Except where specified, all experiments were performed in 20 mM HEPES, pH 7.5, 150 mM KCl and 1 mM dithiothreitol. Nucleosomes were prepared using recombinant *Xenopus laevis* histones with and without a methyl lysine analogue at H3K9. Silencing assays were performed at 30 °C for 2–3 days. The Ab1220 (Abcam) was used for H3K9me2 chromatin immunoprecipitation.

Full Methods and any associated references are available in the online version of the paper.

Received 21 July 2012; accepted 22 February 2013.
Published online 13 March 2013.

1. Eissenberg, J. C. & Elgin, S. C. The HP1 protein family: getting a grip on chromatin. *Curr. Opin. Genet. Dev.* **10,** 204–210 (2000).
2. Lachner, M., O'Carroll, D., Rea, S., Mechtler, K. & Jenuwein, T. Methylation of histone H3 lysine 9 creates a binding site for HP1 proteins. *Nature* **410,** 116–120 (2001).

3. Nakayama, J., Rice, J. C., Strahl, B. D., Allis, C. D. & Grewal, S. I. Role of histone H3 lysine 9 methylation in epigenetic control of heterochromatin assembly. *Science* **292,** 110–113 (2001).
4. Noma, K., Allis, C. D. & Grewal, S. I. Transitions in distinct histone H3 methylation patterns at the heterochromatin domain boundaries. *Science* **293,** 1150–1155 (2001).
5. Grewal, S. I. S. & Jia, S. Heterochromatin revisited. *Nature Rev. Genet.* **8,** 35–46 (2007).
6. Hall, I. M. *et al.* Establishment and maintenance of a heterochromatin domain. *Science* **297,** 2232–2237 (2002).
7. Bannister, A. J. *et al.* Selective recognition of methylated lysine 9 on histone H3 by the HP1 chromo domain. *Nature* **410,** 120–124 (2001).
8. Jacobs, S. A. & Khorasanizadeh, S. Structure of HP1 chromodomain bound to a lysine 9-methylated histone H3 tail. *Science* **295,** 2080–2083 (2002).
9. Nielsen, P. R. *et al.* Structure of the HP1 chromodomain bound to histone H3 methylated at lysine 9. *Nature* **416,** 103–107 (2002).
10. Yamada, T., Fukuda, R., Himeno, M. & Sugimoto, K. Functional domain structure of human heterochromatin protein HP1(Hsa): involvement of internal DNA-binding and C-terminal self-association domains in the formation of discrete dots in interphase nuclei. *J. Biochem.* **125,** 832–837 (1999).
11. Brasher, S. V. *et al.* The structure of mouse HP1 suggests a unique mode of single peptide recognition by the shadow chromo domain dimer. *EMBO J.* **19,** 1587–1597 (2000).
12. Cowieson, N. P., Partridge, J. F., Allshire, R. C. & McLaughlin, P. J. Dimerisation of a chromo shadow domain and distinctions from the chromodomain as revealed by structural analysis. *Curr. Biol.* **10,** 517–525 (2000).
13. Smothers, J. F. & Henikoff, S. The HP1 chromo shadow domain binds a consensus peptide pentamer. *Curr. Biol.* **10,** 27–30 (2000).
14. Mendez, D. L. *et al.* The HP1a disordered C terminus and chromo shadow domain cooperate to select target peptide partners. *Chembiochem* **12,** 1084–1096 (2011).
15. Zhao, T., Heyduk, T., Allis, C. D. & Eissenberg, J. C. Heterochromatin protein 1 binds to nucleosomes and DNA *in vitro*. *J. Biol. Chem.* **275,** 28332–28338 (2000).
16. Keller, C. *et al.* $HP1^{Swi6}$ mediates the recognition and destruction of heterochromatic RNA transcripts. *Mol. Cell* (2012).
17. Wang, G. *et al.* Conservation of heterochromatin protein 1 function. *Mol. Cell. Biol.* **20,** 6970–6983 (2000).
18. Canzio, D. *et al.* Chromodomain-mediated oligomerization of HP1 suggests a nucleosome-bridging mechanism for heterochromatin assembly. *Mol. Cell* **41,** 67–81 (2011).
19. Frigon, R. P. & Timasheff, S. Magnesium-induced self-association of calf brain tubulin. II. Thermodynamics. *Biochemistry* **14,** 4567–4573 (1975).
20. LeRoy, G. *et al.* Heterochromatin protein 1 is extensively decorated with histone code-like post-translational modifications. *Mol. Cell. Proteom.* **8,** 2432–2442 (2009).
21. Sampath, S. C. *et al.* Methylation of a histone mimic within the histone methyltransferase G9a regulates protein complex assembly. *Mol. Cell* **27,** 596–608 (2007).
22. Ruan, J. *et al.* Structural basis of the chromodomain of Cbx3 bound to methylated peptides from histone h1 and G9a. *PLoS ONE* **7,** e35376 (2012).
23. Rice, S. *et al.* A structural change in the kinesin motor protein that drives motility. *Nature* **402,** 778–784 (1999).
24. Dawson, M. A. *et al.* JAK2 phosphorylates histone H3Y41 and excludes HP1α from chromatin. *Nature* **461,** 819–822 (2009).
25. Lavigne, M. *et al.* Interaction of HP1 and Brg1/Brm with the globular domain of histone H3 is required for HP1-mediated repression. *PLoS Genet.* **5,** e1000769 (2009).
26. Richart, A. N., Brunner, C. I. W., Stott, K., Murzina, N. V. & Thomas, J. O. Characterization of chromoshadow domain-mediated binding of heterochromatin protein 1α (HP1α) to histone H3. *J. Biol. Chem.* **287,** 18730–18737 (2012).
27. Sadaie, M., Iida, T., Urano, T. & Nakayama, J.-I. A chromodomain protein, Chp1, is required for the establishment of heterochromatin in fission yeast. *EMBO J.* **23,** 3825–3835 (2004).
28. Sadaie, M. *et al.* Balance between distinct HP1 family proteins controls heterochromatin assembly in fission yeast. *Mol. Cell. Biol.* **28,** 6973–6988 (2008).
29. Mullins, R. D. How WASP-family proteins and the Arp2/3 complex convert intracellular signals into cytoskeletal structures. *Curr. Opin. Cell Biol.* **12,** 91–96 (2000).
30. Huse, M. & Kuriyan, J. The conformational plasticity of protein kinases. *Cell* **109,** 275–282 (2002).

Supplementary Information is available in the online version of the paper.

Acknowledgements We thank J. Tretyakova for preparation of histone proteins and J. Leonard for sample preparation for cryo-electron microscopy of nucleosome alone. We thank W. Lim, M. Simon, K. Armache, J. Zalatan, L. Racki and members of the Narlikar laboratory for discussions. D.C. would like to thank I. Ortiz Torres and K. M. Kuchenbecker for scientific discussions and members of the Schuck laboratory for advice on AUC approaches. This work was supported by a grant from the Hillblom foundation to D.C., by grants from the American Cancer Society and Leukemia and Lymphoma Society to G.J.N., National Institutes of Health (NIH) grant R01GM071801 to H.D.M. and by a New Technology Award to Y.C. from the UCSF Program for Breakthrough Biomedical Research. P.S. was supported by the Intramural Research Program of the NIBIB, NIH. N.N. and E.P. were supported by the NIH grant AR053720.

Author Contributions D.C. and G.J.N. identified, developed and addressed the core questions. D.C. performed the bulk of the experiments. P.S. trained D.C. in the use of AUC approaches and was instrumental in interpreting the AUC data. N.N. performed the EPR experiments. D.B.M. trained D.C. in strain construction and in the use of *S. pombe* assays. J.F.G. constructed some of the *S. pombe* strains and performed initial *in vivo* experiments. E.P., R.C., A.L. and D.C. deconvolved the EPR spectra. S.W. generated the cryo-electron-microscopy reconstruction of the nucleosome alone. M.L. generated the EM reconstructions of the Swi6–nucleosome complex and the two-dimensional reconstructions of the CFP–Swi6 and Swi6–CFP constructs. M.L., S.W. and Y.C. analysed the electron microscopy data. Y.C. oversaw all of the electron microscopy studies. H.D.M. oversaw the design and interpretation of the *in vivo* experiments. R.C. oversaw the EPR analysis and interpretation. D.C. and G.J.N. wrote the bulk of the manuscript with substantial intellectual contributions from R.C.

Author Information Reprints and permissions information is available at www.nature.com/reprints. The authors declare no competing financial interests. Readers are welcome to comment on the online version of the paper. Correspondence and requests for materials should be addressed to G.J.N. (geeta.narlikar@ucsf.edu).

METHODS

Protein cloning and purification. Swi6 proteins were purified from *Escherichia coli* as described previously[18]. Except for the CFP-tagged proteins, all other Swi6 protein purifications yield final proteins that are devoid of N- or C-terminal tags. Protein concentrations of all Swi6 construct samples were measured by ultraviolet absorption at 280 nm and calculated using the experimentally determined extinction coefficient (see AUC section). To ensure that there was minimal DNA contamination, we measured the 260/280 ratio for every purified protein, which on average was ~0.5.

Reaction buffer conditions. Except where specified, all experiments were performed in the reaction buffer consisting of 20 mM HEPES, pH 7.5, 150 mM KCl and 1 mM dithiothreitol.

Nucleosome assembly. Core nucleosomes were assembled on 147 base pairs (bp) of DNA using the 601 positioning sequence, containing a Pst1 site 18 bp in from the 5′ end. For the cryo-electron microscopy of nucleosome-alone studies, 207 bp of DNA containing the 601 sequence at one end was used. All nucleosomes were prepared using recombinant *Xenopus laevis* histones and assembled as described previously[31]. Methyl lysine analogue containing H3 histones at position 9 ($H3K_C9me3$) were prepared as described previously[32].

Tryptophan fluorescence studies. The association between Swi6 proteins and the H3 peptides (amino acids 1–18) were measured following the increases in the internal fluorescence of Trp 104 (one of the three residues in the aromatic cage) using an ISS K2 fluorimeter at 30 °C. Samples containing 200 nM Swi6 in reaction buffer were mixed with increasing concentrations of each H3 peptide, trimethylated or unmethylated at lysine 9. After an incubation for 10 min at 30 °C, the fluorescence of Trp 104 was measured with the incident wavelength of 295 nm. The observed fluorescence intensity (F_{obs}) at 330 nm was plotted as a function of peptide concentration. A 1:1 binding model was fit to the data using GraphPad Prism and the following set of equations:

$$F_{obs} = \frac{(F_{max}[H3_p + F_{min}K_d)}{([H3_p + K_d)}$$

in which F_{max} is the fluorescence at saturating peptide, F_{min} is the fluorescence in the absence of peptide and $H3_p$ represents the H3 tail peptide. The obtained dissociation constant (K_d) values were averaged over three independent sets of data.

Fluorescence polarization studies. Fluorescence polarization-based measurements of binding to H3 tail peptides (amino acids 1–15), DNA and nucleosomes were performed in reaction buffer with 0.01% NP-40 at 24 °C. In total, 5–10 nM of peptide, DNA or nucleosomes were used and Swi6 concentrations were varied. The binding reaction was incubated for 30 min at 24 °C and fluorescence polarization was measured using an Analyst HT (Molecular Devices) with excitation and emission wavelengths of $\lambda_{ex} = 480$ nm and $\lambda_{em} = 530$ nm, respectively. The H3 peptide was labelled at the N terminus with a fluorescein probe (FAM). The peptide was synthesized by GenScript. The 20-base-pair DNA used in the DNA-binding assay was 5′-labelled with 5,6 carboxy-fluorescein (IDT). The DNA to assemble fluorescent nucleosomes was labelled on one end by amplifying the sequence using PCR with a primer covalently linked to 6-carboxyfluorescein by a 6-carbon linker (IDT). All data were analysed using GraphPad Prism.

The peptide and DNA-binding data were fit by the following equation:

$$F_{obs} = \frac{(F_{max}[Swi6 + F_{min}K_d)}{([Swi6 + K_d)}$$

In which F_{obs} is the fluorescence polarization signal observed, F_{min} is the fluorescence polarization signal for the probe alone (peptide or DNA) and F_{max} is the fluorescence polarization signal at saturating [Swi6]. The obtained K_d values were averaged over three or more independent sets of data.

The following model was used to fit the nucleosome-binding data to account for Swi6–Swi6 oligomerization that is scaffolded by the Swi6–nucleosome complex. Because the fluorescent probe is located only on one end of the DNA (asterisks), we made the assumption that changes in fluorescence polarization reflect binding of Swi6 on one side of the nucleosome. We proposed that binding to the other side occurs independently and is invisible to our assay:

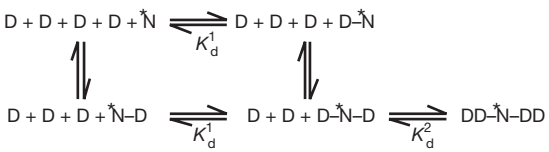

In which D indicates a Swi6 dimer, D–N–D is the Swi6–nucleosome complex and DD–N–DD is the Swi6–nucleosome complex bound by additional Swi6 dimers. The fluorescence polarization nucleosome data were fitted using the following equation:

$$F_{obs} = \frac{(F_0K_d^1K_d^2 + F_1[Swi6\ K_d^2 + F_2[Swi6\ ^2)}{(K_d^1K_d^2 + [Swi6\ K_d^2 + [Swi6\ ^2)}$$

In which F_{obs} is the fluorescence polarization signal observed, F_0 is the fluorescence polarization signal for the nucleosome alone, F_1 is the fluorescence polarization signal of the saturated Swi6–nucleosome complex, F_2 is the fluorescence polarization signal due to the oligomerization of Swi6 scaffolded by the Swi6–nucleosome complex, K_d^1 is the dissociation constant for the Swi6–nucleosome complex and K_d^2 is the dissociation constant for Swi6–Swi6 scaffolded by the Swi6–nucleosome complex. Data comparing $Swi6^{WT}$ to the mutants were globally analysed: the F_0, F_1 and F_2 were fixed among all proteins whereas the K_d^1 and K_d^2 were floated.

AUC studies. Swi6 proteins were individually dialysed into reaction buffer overnight. Swi6 proteins were quantified by ultraviolet absorption at 280 nm. We experimentally determined the $Swi6^{WT}$ extinction coefficient by recording both interference fringes and ultraviolet absorbance at 280 nm for a given Swi6 sample. We then converted the number of interference fringes observed into milligrams of Swi6 per millilitre using an average refractive increment of 4.1 fringes mg^{-1} ml. Using this estimated concentration and the absorbance value at 280 nm, we then calculated the extinction coefficient at 280 nm to be 36,880 M^{-1} cm^{-1}. Simultaneous detection of protein by ultraviolet absorbance at multiple wavelengths allowed for the determination of the extinction coefficients at 230 nm and 250 nm (13,650 M^{-1} cm^{-1} and 221000 M^{-1} cm^{-1}, respectively).

All sedimentation experiments were conducted using an analytical ultracentrifuge (Beckman Coulter) equipped with either sole absorption optical scanner (Optima XLA) or both absorption and interference optics scanner (Optima XLI). Data were acquired with ProteomeLab data acquisition software 5. Global analysis of sedimentation equilibrium and sedimentation velocity isotherm data was performed using the SEDPHAT software. Error estimates were calculated on the basis of replicates of three or more experiments and confidence intervals based on F-statistics and the error projection method. Partial-specific volume (ν), solution density (ρ) and solution viscosity (η) were calculated in SEDNTERP.

Sedimentation equilibrium. Sedimentation equilibrium experiments were conducted at 8 °C in an Optima XLI/A at rotor speeds of 6,000, 11,000 and 18,000 r.p.m. in double-sector centrepieces with sample volumes of 170 µl. Loading concentration of Swi6, in monomer units, was varied from 1.7 µM to 32 µM. Absorbance data, at wavelengths of 280, 250 and 230 nm, and immunofluorescence data were acquired from samples at five different loading concentrations at all rotor speeds. Global analysis of data at different wavelengths and rotor speeds was conducted with the software SEDPHAT, using Boltzmann exponentials representing the predicted concentration profiles of each species in chemical equilibrium, with amplitudes at all radii constrained by the mass action law:

$$c_{tot} = c_1 + nKc_1^n + \sum_{i=1}^{\infty}(n+im)Kc_1^n(Lc_1^n)^i$$

in combination with the method of implicit mass conservation, using the bottom position of each solution column as an adjustable parameter. In the above equation, c_{tot} is the total protein concentration, c_1 is the concentration of Swi6 monomer, n is the number of Swi6 subunits that self-associate in the first-step of association ($n = 2$ for dimer formation), m is the molecularity of the chain-elongation unit ($m = 2$ for a dimeric chain-elongation unit), K is the association constant for Swi6 dimerization (K_{obs}^{dim}), L is the association constant for Swi6 isodesmic chain elongation (K_{obs}^{iso}) and i is the number of units of m added to the initial complex formed by self-association of n Swi6 subunits[33]. Summation of terms was carried out to a relative numerical precision of 10^{-6}.

Sedimentation velocity. Samples volumes of 400 µl at an overall final optical density (OD) between 0.1 and 1.0, were pipetted into double-sector centrepieces and inserted in an eight-hole rotor, which was placed in the temperature pre-equilibrated AUC chamber. An additional incubation period of 1–2 h was added with the rotor at rest and under vacuum for temperature equilibration. For experiments performed at 4 °C, the samples were left equilibrating under vacuum overnight. Runs were performed at a rotor speed of 50,000 r.p.m. for more than 12 h. Scans were collected following ultraviolet absorption at 230, 250 and 280 nm, scanned with a radial step size of 0.003 cm in continuous mode, and/or using the interference system. Data were analysed using a $c(s)$ continuous distribution of Lamm equation solutions with the software SEDFIT, followed by integration and assembly into an isotherm of weighted-average s-values. The isotherm was modelled in SEDPHAT with mass-action-based models for the weighted-average s-value

$$s_w(c_{tot}) = [c_1 s_1 + nKc_1^n s_n + \sum_i \left((n+im)Kc_1^n (Lc_1^m)^i s_n \left(\frac{n+im}{n} \right)^k \frac{1}{c_{tot}} (1 - k_s c_{tot} m_1) \right)$$

assuming a power law for the sedimentation coefficients of oligomeric species with $\kappa = 0.566$ (consistent with increasingly elongated oligomers; this value was predetermined from the global fit of sedimentation equilibrium and sedimentation velocity on an extensive data set), in combination with an overall hydrodynamic non-ideality term of magnitude $k_s = 0.01\ \mathrm{ml\ g^{-1}}$. As in the equation above, c_{tot} is the total protein concentration, c_1 is the concentration of Swi6 monomer, n is the number of Swi6 subunits that self-associate in the first-step of association ($n = 2$ for dimer formation), m is the molecularity of the chain elongation unit ($m = 2$ for a dimeric chain elongation unit), K is the association constant for Swi6 dimerization (K_{obs}^{dim}), L is the association constant for Swi6 isodesmic chain elongation (K_{obs}^{iso}), s_1 is the sedimentation coefficient of Swi6 monomer and s_n is the sedimentation coefficient of Swi6 dimer ($n = 2$).

Rationale for different temperatures. (1) To obtain a model for Swi6 self-association we performed sedimentation equilibrium and sedimentation velocity AUC studies at 8 °C. Sedimentation equilibrium experiments are ~1 week long, so a temperature of 8 °C was used to stabilize the protein. Global analysis of both sedimentation equilibrium and sedimentation velocity AUC at 8 °C allowed us to obtain a thermodynamic information for Swi6 self-association as well as hydrodynamic parameters for Swi6 monomer, dimer and oligomers that were used in all the sedimentation velocity experiments performed at higher temperatures. (2) To compare dimerization properties between Swi6 mutants, we had to perform the experiments at 30 °C because dimerization is too tight at lower temperatures. (3) To stabilize probe-labelled Swi6 proteins, the EPR and AUC experiments were done at 4 °C.

EPR studies. EPR measurements were performed with an EMX EPR spectrometer (Bruker Instruments). First derivative, X-band spectra were recorded in a high-sensitivity microwave cavity using 50-s, 100-G wide magnetic field sweeps. The instrument settings were as follows: microwave power, 25 mW; time constant, 164 ms; frequency, 9.83 GHz; modulation, 1 G at a frequency of 100 kHz. Each spectrum used in the data analysis was an average of 10–40 50-s sweeps from an individual experimental preparation. Swi6^{3S} was labelled by reacting the sole cysteine residue (either K94C or G95C) with the EPR probe 4-maleimido-2,2,6,6-tetramethyl-1-piperidinyloxy (MSL, Sigma Aldrich). The protein was first dialysed overnight in reaction buffer without dithiothreitol. It was then incubated with MSL using a twofold molar excess of MSL to protein concentration. The mixture was then left to react for 4 h at 4 °C. The excess label was removed by a microcon concentrator, followed by an additional overnight dialysis step into the above buffer. The protein sample was incorporated into a 25-µl capillary and the EPR spectrum was recorded. The temperature of the sample was controlled by blowing dry air (warm or cool) into the cavity and monitored using a thermistor placed close to the experimental sample. To stabilize the Swi6$^{probe-WT}$ and Swi6^{probe} mutants we performed the EPR and AUC experiments at 4 °C.

The spectra were deconvoluted into mobile and immobile spectral components using the protocols described in ref. 34.

Electron microscopy and image processing. Negative-stain electron microscopy of CFP–Swi6 and Swi6–CFP. Proteins were dialysed overnight in reaction buffer. In total, 2.5 µl of CFP–Swi6 at 0.34 µM and of Swi6–CFP at 0.1 µM was absorbed to a glow-discharged copper grid coated with carbon film for 30 s followed by conventional negative stain with 0.75% uranyl formate. Images were collected using a Tecnai T12 microscope (FEI Company) with a LaB_6 filament and operated at 120-kV accelerating voltage. All images were recorded at a magnification of ×67,000 with an UltraScan 4096 × 4096 pixel CCD camera (Gatan).

All images were 2 × 2 pixel binned to the final pixel size of 3.46 Å before any further processing. A total of 5,000 and 3,000 particles for CFP–Swi6 and Swi6–CFP, respectively were selected from ~50 images using the display program SAMViewer (written by M. Liao). All subsequent image processing was performed using Spider[35] and Frealign.

Cryo-electron microscopy studies of the nucleosome and Swi6–nucleosome complex. Cryo-electron microscopy data were collected using Tecnai TF20 electron microscope equipped with a field emission gun (FEI Company) and operated at 120 kV (for the nucleosome) or at 200 kV (for the Swi6–nucleosome complex). Images were collected at a nominal magnification of ×62, 000 using a TemF816 8K × 8K CMOS camera (TVIS).

Nucleosome alone. The nucleosome contained 60 bp of flanking DNA (147 bp of 601 sequence + 60 bp extra DNA) and did not contain the methyl lysine analogue on H3K9. All images were binned by a factor of 2 (2.39 Å/pixel) for further processing. Defocus values were determined for each micrograph using CTFFIND[37] and ranged from −1.5µm to −3 µm. A total of 13,629 particles were selected and classified into 100 two-dimensional class averages. Three-dimensional reconstructions were calculated and refined using GeFREALIGN[36]. The initial model was generated by filtering the atomic structure of the nucleosome (PDB code, 1KX5) to 35 Å (command pdb2mrc from EMAN package)[38]. The resolution was estimated to be ~16.5 Å, on the basis of Fourier shell correlation (FSC) = 0.5 criteria.

Swi6–H3K$_C$9me3 nucleosome complex. Swi6 was dialysed overnight in reaction buffer. The binding reaction was set such that, first, both nucleosome and Swi6 concentrations were above the K_d value measured by fluorescence polarization (FP) and second, the Swi6 concentration was sufficient to titrate all the nucleosomes as assayed by native gel shift. Those same conditions were used previously to measure the stoichiometry of the complex by sedimentation velocity AUC and are known to result in homogenous samples[18].

A total of 5,000 particles were selected and classified into 200 two-dimensional class averages and all were included in the final three-dimensional reconstruction. The cryo-electron microscopy three-dimensional reconstruction of the nucleosome alone was low-pass filtered to 35 Å and used as the initial model for three-dimensional refinement of the complex. We used our previous biochemical knowledge to guide the structural analysis. We have previously shown that the complex of Swi6 with an H3K9 methylated nucleosome contains two Swi6 dimers[18]. Given the pseudo-two-fold symmetry in the positions of the H3 tails, the simplest model posits that the Swi6 dimers also bind in a pseudo-symmetric manner with one dimer on either side of the nucleosome. Indeed in some of the two-dimensional class averages we observe density on either side of the nucleosome consistent with the predictions of the biochemical analysis (Supplementary Fig. 7). We therefore applied two-fold symmetry to obtain the three-dimensional reconstruction. The resolution of the final three-dimensional reconstruction was estimated to be ~25 Å, on the basis of FSC = 0.5 criteria. This same resolution was also obtained when the cryo-electron microscopy three-dimensional reconstruction of nucleosome alone was low-pass filtered to 60 Å.

All three-dimensional reconstructions were visualized by UCSF Chimera. The 'Fit in Map' function of Chimera was used to dock the atomic structure of the nucleosome (PDB code, 1KX5) into the three-dimensional volume[39].

To calculate the difference map, the nucleosome alone and the Swi6–nucleosome complex maps were low-pass filtered to 25 Å. The difference map was calculated by subtracting the nucleosome from the Swi6–nucleosome complex using the program diffmap.exe (provided by N. Grigorieff), which normalizes the density maps before calculating the difference map. The extended shape of the difference density is compatible with the shape of the Swi6 dimer visualized in the negatively stained CFP–Swi6 dimer (Fig. 3a). Such similarity suggested a model for the arrangement of the individual domains of Swi6 and enabled us to manually place the known crystal structures of the CD and CSD into the difference density (Fig. 3d).

Silencing assays. The strains were grown overnight to saturation and diluted to $OD_{600\ nm}$ of 1 at the highest dilution. Serial dilutions were performed with dilution factor of 5 and cells were grown on non-selective (YS)- and 5-FOA (2 g l^{-1} 5-fluoroorotic acid)-containing media for *ura4*$^+$ reporter at 30 °C for 2–3 days.

Quantifying Swi6 protein levels *in vivo*. Swi6 protein levels were quantified using polyclonal antibodies raised in rabbits by injecting recombinant Swi6.

Chromatin immunoprecipitation. The chromatin immunoprecipitation assay was performed as described previously[40]. Cells were lysed at 4 °C by bead beating seven times for 1 min each with 2-min rests on ice. Chromatin fraction was sonicated 20 times for 30 s, each with a 1-min rest in between cycles using Bioruptor. Ab1220 (Abcam) was used for H3K9me2 chromatin immunoprecipitation and protein A Dynabeads were used in the washing steps.

31. Luger, K., Rechsteiner, T. J. & Richmond, T. J. Preparation of nucleosome core particle from recombinant histones. *Methods Enzymol.* **304,** 3–19 (1999).
32. Simon, M. D. Installation of site-specific methylation into histones using methyl lysine analogs. *Curr. Protocols Mol. Biol.* Ch 21:Unit 21.18.1–10 (2010).
33. Vistica, J. *et al.* Sedimentation equilibrium analysis of protein interactions with global implicit mass conservation constraints and systematic noise decomposition. *Anal. Biochem.* **326,** 234–256 (2004).
34. Purcell, T. J. *et al.* Nucleotide pocket thermodynamics measured by EPR reveal how energy partitioning relates myosin speed to efficiency. *J. Mol. Biol.* **407,** 79–91 (2011).
35. Frank, J. *et al.* SPIDER and WEB: processing and visualization of images in 3D electron microscopy and related fields. *J. Struct. Biol.* **116,** 190–199 (1996).
36. Li, X., Grigorieff, N. & Cheng, Y. GPU-enabled FREALIGN: accelerating single particle 3D reconstruction and refinement in Fourier space on graphics processors. *J. Struct. Biol.* **172,** 407–412 (2010).
37. Mindell, J. A. & Grigorieff, N. Accurate determination of local defocus and specimen tilt in electron microscopy. *J. Struct. Biol.* **142,** 334–347 (2003).

38. Ludtke, S. J., Baldwin, P. R. & Chiu, W. EMAN: semiautomated software for high-resolution single-particle reconstructions. *J. Struct. Biol.* **128,** 82–97 (1999).
39. Pettersen, E. F. *et al.* UCSF Chimera–a visualization system for exploratory research and analysis. *J. Comput. Chem.* **25,** 1605–1612 (2004).
40. Rougemaille, M., Shankar, S., Braun, S., Rowley, M. & Madhani, H. D. Ers1, a rapidly diverging protein essential for RNA interference-dependent heterochromatic silencing in *Schizosaccharomyces pombe*. *J. Biol. Chem.* **283,** 25770–25773 (2008).